第38卷第4期 红外与毫米波学报 Vol. 38, No. 4
2019年8月 J. Infrared Millim. Waves August, 2019

文章编号: 1001-9014(2019)04-0445-06 DOI:10.11972/j.issn.1001-9014.2019.04.009

Nonlocality-induced polarization beam splitting via metal-dielectric composites

WANG Dun-Jian[1], LI Su-Cheng[2,3], JI Wen-Jie[1], XIONG Wei[2], ZHANG Lei[2], SHANG Yuan-Fang[2*], LUO Jie[1,4]

(1. School of Physical Science and Technology, Soochow University, Suzhou 215006, China;
2. Shenzhen Kuang-Chi Institute of Advanced Technology, Shenzhen 518000, China;
3. Shenzhen Kuang-Chi Cutting-edge Technology Co., Ltd, Shenzhen 518000, China;
4. State Key Laboratory of Meta-RF Electromagnetic Modulation Technology, Shenzhen 518000, China)

Abstract: Three kinds of polarization beam splitters are designed by using a simple metal-dielectric multilayered structure with strong nonlocality. It is found that the equal frequency contour for the transverse electric polarization is a small circle when the average permittivity is close to zero. At the same time, the equal frequency contour for the transverse magnetic polarization turns to be two branches of parabolas due to the surface plasmon-induced nonlocal effect. Based on the dramatic difference between dispersions of the two polarizations, three kinds of polarization beam splitters are demonstrated, including the ultrathin ones, which may have important applications in polarization-sensitive absorbers and compact optical devices.

Key words: nonlocality, polarization beam splitters, zero-index media, metal-dielectric composites
PACS: 41.20.Jb, 78.20.Ci, 73.20.Mf

金属-电介质复合材料中非局域效应诱导的偏振分光器

王敦建[1], 李肃成[2,3], 季文杰[1], 熊 伟[2], 张 磊[2], 商院芳[2*], 罗 杰[1,4]

(1. 苏州大学 物理科学与技术学院,江苏 苏州 215006;
2. 深圳光启高等理工研究院,广东 深圳 518000;
3. 深圳光启尖端技术有限责任公司,广东 深圳 518000;
4. 超材料电磁调制技术国家重点实验室,广东 深圳 518000)

摘要:基于具有强非局域效应的金属-电介质多层膜结构提出了三种偏振分光器.当多层膜结构的平均介电常数为零时,横电偏振电磁波对应的等频率曲线为一很小的圆,而横磁偏振电磁波对应的等频率曲线则为两支抛物线,这是由表面等离激元诱导的非局域效应引起的.利用该多层膜结构在不同偏振电磁波下等频率曲线表现出巨大差异这一特性,提出了三种偏振分光器,其中包含厚度远小于波长的超薄偏振分光器.这些结果有望在偏振选择吸收体以及集成光子器件中有潜在应用.

关 键 词:非局域效应;偏振分光器;零折射率材料;金属-电介质复合材料

中图分类号:O436 **文献标识码**:A

Introduction

Metamaterials composed of subwavelength microstructures generally can be homogenized to effective media characterized by local effective parameters, i. e., without spatial dispersion[1-4]. However, interestingly, the effective parameters of some metamaterials containing metallic components are found to be nonlocal, i. e., spatially dispersive, even when the microstructures are in deep-subwavelength scale[5-29]. Therefore, traditional effective medium theories (EMTs) predicting the local effective parameters fail to homogenize such metamaterials. As we know, the traditional EMTs usually require relatively uniform fields inside and between the microstructures[30-31]. But in metallic structures, surface plasmons may be excited, resulting in drastically varying fields inside and between the microstructures. As a conse-

---

Received date: 2018-11-25, **revised date**: 2019-05-29 **收稿日期**:2018-11-25, **修回日期**:2019-05-29
Foundation items: Supported by the Shenzhen Science and Technology Plan (JSGG20160819150017627, JSGG20160819150000459)
Biography: WANG Dun-Jian (1994-), male, Xuzhou, China. Master. Research area involves zero-index metamaterials and coherent perfect absorption. E-mail: djvanoliver@163.com
* **Corresponding author**: E-mail: yuanfang.shang@kuang-chi.com

quence, the nonlocality may appear in the effective parameters, thich brings rich and colorful effects and applications beyond the local framework of metamaterials. In particular, the nonlocality becomes even stronger in the zero-index media with the permittivity or/and permeability near zero[20-28, 32-34], yielding unique properties and applications like parabolic dispersion[20-23], additional extraordinary waves[24-25], all-angle negative refraction and subwavelength imaging[23], etc.

On the other hand, polarization beam splitters (PBSs), which separate two orthogonal polarizations of light into different propagation directions, are very important and widely used in polarization manipulation, optical communication, data storage, image processing and display. Traditional PBSs are based on either Brewster effect or natural crystal birefringence, which requires a large thickness to obtain enough walk-off distance between the two polarizations as the birefringence of a natural material is always small[35]. With the development of photonic crystals, metamaterials and metasurfaces, novel methods have been proposed[35-55]. For instance, based on photonic crystals, polarization-dependent dispersions[35, 37-40] or bandgaps at different wavelength range for two polarizations[41-43] can be achieved to split transverse electric (TE) and transverse magnetic (TM) polarizations. The strong anisotropy in metamaterials can mitigate the design of PBSs[47-48]. Gradient metasurfaces can introduce different additional phases to different polarizations to separate the two polarizations[49-50]. In addition, broadband PBSs and polarization rotators can be realized based on multi-wave interference in multilayered meta-grating structures[53-54].

In this paper, we propose to use a simple metal-dielectric multilayered structure with nonlocal effects to realize three kinds of PBSs. We find that when the average permittivity of the multilayer is near zero, the nonlocal effect become dramatic. This leads to a great difference in dispersions of TE and TM polarizations, enabling the separation of two polarizations.

1 Dispersions and polarization beam splitters

To begin with, we investigate the dispersions of metal-dielectric multilayered structure, as illustrated in Fig. 1(a). Such a multilayer is a periodic stacking of metal and dielectric layers with a lattice constant of . Based on the transfer matrix methods, the dispersions for TE and TM polarizations can be, respectively, expressed as:

$$\cos(k_y a) = \cos(f_d p_y a)\cosh(f_m q_y a) - \frac{1}{2}\left(\frac{p_y}{q_y} - \frac{q_y}{p_y}\right)\sin(f_d p_y a)\sinh(f_m q_y a) \quad ,(1)$$

and

$$\cos(k_y a) = \cos(f_d p_y a)\cosh(f_m q_y a) - \frac{1}{2}\left(\frac{\varepsilon_m p_y}{\varepsilon_d p_y} - \frac{\varepsilon_d q_y}{\varepsilon_m p_y}\right)\sin(f_d p_y a)\sinh(f_m q_y a) \quad ,(2)$$

where $p_y = \sqrt{\varepsilon_d k_0^2 - k_x^2}$, $q_y = \sqrt{k_x^2 - \varepsilon_m k_0^2}$. $k_0\ (=2\pi/\lambda_0)$ and λ_0 are the wave number and wavelength in free space, respectively. $\varepsilon_d(f_d)$ and $\varepsilon_m(f_m)$ are the relative permittivity (filling ratio) of the dielectric and metal layers, respectively. Here we have the relation $f_d + f_m = 1$.

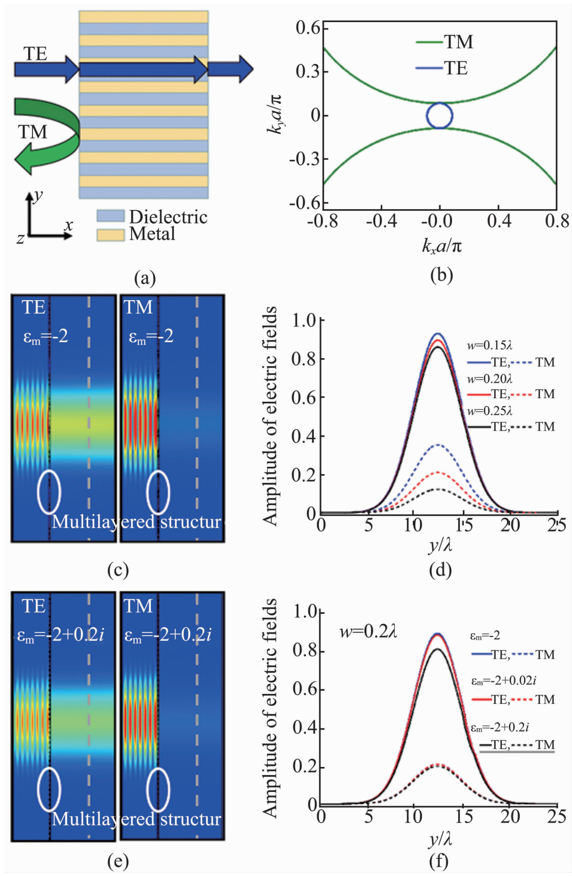

Fig. 1 (a) Schematic of the first kind of PBS. (b) The EFCs for TE (blue lines) and TM (green lines) polarizations. [(c) and (e)] Amplitude of electric fields for TE (left) and TM (right) polarized waves under normal incidence when the relative permittivity of metal is (c) $\varepsilon_m = -2$, (e) $\varepsilon_m = -2 + 0.2i$. The thickness of the multilayered structure is $w = 0.20\lambda$. (d) The distribution of amplitude of electric fields along the dashed lines in (c) for TE (solid lines) and TM (dashed lines) polarizations when the thickness is set to be $w = 0.15\lambda$ (blue lines), $w = 0.20\lambda$ (red lines) and $w = 0.25\lambda$ (black lines). (f) The distribution of amplitude of electric fields along the dashed lines in (e) for TE (solid lines) and TM (dashed lines) polarizations when the relative permittivity of metal is $\varepsilon_m = -2$ (blue lines), $\varepsilon_m = -2 + 0.02i$ (red lines) and $\varepsilon_m = -2 + 0.2i$ (black lines). The relevant parameters are $\varepsilon_d = 6$, $f_m = 0.75$ and $a = \lambda/6$

图 1 (a)第一类偏振分光器的示意图.(b)TE 偏振(蓝色曲线)和 TM 偏振(绿色曲线)下的等频率曲线.[(c)和(e)]TE 偏振(左图)和 TM 偏振(右图)电磁波正入射时的电场振幅分布图,其中(c)中 $\varepsilon_m = -2$,(e)中 $\varepsilon_m = -2 + 0.2i$. 多层结构的厚度为 $w = 0.20\lambda$.(d)沿着(c)中虚线上的电场振幅分布图,其中实线和虚线分别代表 TE 偏振和 TM 偏振,蓝色、红色和黑色曲线分别对应于多层结构厚度为 $w = 0.15\lambda$、$w = 0.20\lambda$ 和 $w = 0.25\lambda$ 的情形.(f)沿着(e)中虚线上的电场振幅分布图,其中实线和虚线分别代表 TE 偏振和 TM 偏振,蓝色、红色和黑色曲线分别对应于金属相对介电常数为 $\varepsilon_m = -2$、$\varepsilon_m = -2 + 0.02i$ 和 $\varepsilon_m = -2 + 0.2i$ 的情形. 其它相关参数为 $\varepsilon_d = 6$, $f_m = 0.75$ 和 $a = \lambda/6$

Assuming that the lattice constant is much smaller than the working wavelength, thus, the trigonometric functions in Eqs. (1-2) can be simplified by using the relation $x \approx x$ and $\cos x \approx 1 - \frac{1}{2!}x^2$. Then, Eqs. (1-2) are reduced to,

$$k_x^2 + k_y^2 \approx \varepsilon_{\parallel} k_0^2 \quad , \quad (3)$$

and,

$$\frac{k_x^2}{\varepsilon_{\perp}} + \frac{k_y^2}{\varepsilon_{\parallel}} \approx k_0^2 \quad , \quad (4)$$

where $\varepsilon_{\parallel}$ ($= \varepsilon_d f_d + \varepsilon_m f_m$) and $\varepsilon_{\perp}$ ($= \varepsilon_d \varepsilon_m / (\varepsilon_d f_m + \varepsilon_m f_r)$) are the average permittivities in the xz plane and y direction, respectively. Actually, they correspond to the local effective parameters predicted by traditional EMTs[30-31].

In particular, if $\varepsilon_{\parallel} = 0$, then Eqs. (1-2) indicate that the equal frequency contours (EFCs) of TE and TM polarizations are a point and a line, respectively. Evidently, they are not physical. In fact, in the case of $\varepsilon_{\parallel} = 0$, one higher order term of the trigonometric functions should be considered, i. e. $\sin x \approx x - \frac{1}{3!}x^3$ and $\cos x \approx 1 - \frac{1}{2!}x^2 + \frac{1}{4!}x^4$. Thus, Eqs. (1-2) are rewritten as,

$$k_x^2 + k_y^2 \approx \frac{a^2}{12} f_d^2 \varepsilon_d^2 k_0^4 - \frac{a^2}{12}[f_d^4 + f_m^4 + 4 f_d f_m (f_d^2 + f_m^2)] k_x^4 \quad , \quad (5)$$

$$\text{and } k_y \approx \pm \frac{a f_d \varepsilon_d}{2\sqrt{3}} \left(k_0^2 - \frac{k_x^2}{\varepsilon_{\perp}} \right) \quad . \quad (6)$$

Equations (5-6) indicate that the EFCs of TE and TM polarizations, respectively, are a small circle and two branches of parabolas (see Fig. 1(b)), which are quite different from those obtained from Eqs. (3-4). This reveals that the traditional EMTs fail to describe the multilayered structure with $\varepsilon_{\parallel}$, and the effective parameters are not local any more. Especially for the TM polarization, the dispersion is drastically different from the local one, which actually is caused by the strong nonlocality induced by the surface plasmons at metal/dielectric surfaces[20-28].

In the numerical calculations, the relevant parameters are $\varepsilon_d = 6$, $\varepsilon_m = -2$, $f_m = 0.75$ and $a = \lambda/6$. From the EFCs in Fig. 1(b), we can see that TE polarized waves under normal incidence onto the yz plane of the multilayered structure can be transmitted, while TM polarized waves would be reflected due to the bandgap, as illustrated in Fig. 1(a). Bases on such a difference, TE and TM polarizations can be separated. Thus, one kind of PBSs can be realized.

To verify such PBSs, numerical simulations are performed by using finite-element software COMSOL Multiphysics. In the left and right figures of Fig. 1(c), TE and TM polarized waves are normally incident from air onto the multilayered structure, whose thickness is $w = 0.20\lambda$ in the x direction. The amplitude of the incident electric field is 1 V/m. The simulation results show that most TM polarized waves can propagate through the multilayered structure, while TE polarized waves are mostly reflected. Furthermore, in Fig. 1(d), we plot the amplitude of electric fields for TE (solid lines) and TM (dashed lines) polarizations along the dashed lines in Fig. 1(c). It is seen that the transmission decreases as the increase of the thickness of the multilayered structure. And the transmission contrast of the two polarizations can be enlarged by the increasing the thickness to block the TM polarization. For example, when the thickness is increased to $w = 0.25\lambda$, the transmission coefficient for the TM polarization is around 0.1 (see Fig. 1(d)). On the other hand, the loss of transmission for the TE polarization is mainly due to the impedance mismatch between air and the multilayered structure, which can be relieved by using appropriate antireflection coatings[56-58].

Moreover, we consider material loss effects on the performance of the PBS. In Fig. 1(e), we re-simulate the distributions of electric-field amplitudes under both TE (left inset) and TM (right inset) polarizations when the relative permittivity of the metal component is set to be . Compared with Fig. 1(c), we can see that although the transmission is decreased a bit due to material losses, the transmission contrast of the two polarizations is still quite large. In Fig. 1(f), we plot the electric-field amplitudes along the dashed lines in Fig. 1(e) for TE (solid lines) and TM (dashed lines) polarizations when the relative permittivity of metal component is (blue lines), (red lines) and (black lines). These results reveal that the PBS can still work well in the existence of material losses.

It is worth noting that the thickness of such a PBS is much smaller than the working wavelength, as we have shown above. Such an ultrathin PBS may be more useful in compact optical devices compared with the previously proposed PBSs[47].

Now, we rotate the multilayered structure, so that the waves are incident onto the plane. Then, we can get different refractive behaviors of the two polarizations, as illustrated in Fig. 2(a). Such a difference in the refractive behaviors enables another kind of PBSs. Therefore, we can obtain different kinds of PBSs by using the same multilayered structure when waves are incident onto the different surfaces.

Specifically, positive and negative refractions occur for the TE and TM polarizations, respectively, as seen from the EFCs in Fig. 2(b). The arrows denote the directions of group velocities of incident and refracted beams. Simulation results under an incident angle of 10 deg are presented in Fig. 2(c), showing positive refraction for the TE polarization (left) and negative refraction for the TM polarization (right). In Fig. 2(c), the color (arrows) denotes the magnitude (direction) of the time-averaged power flow. We notice that almost all the incident waves are transmitted through the multilayered structure irrespective of the polarizations. Moreover, in Fig. 2(d), we plot the time-averaged power flow along the dashed lines in Fig. 2(c). The solid and dashed lines in Fig. 2(d) denote the lossless case with and the lossy case with , respectively. We can clearly see a large walk-off distance in the direction for the two polarizations, thus making it possible to separate the two polarizations. We note that such a walk-off distance can be further enlarged by increasing the thickness of the multilayered structure, or increasing the incident angle.

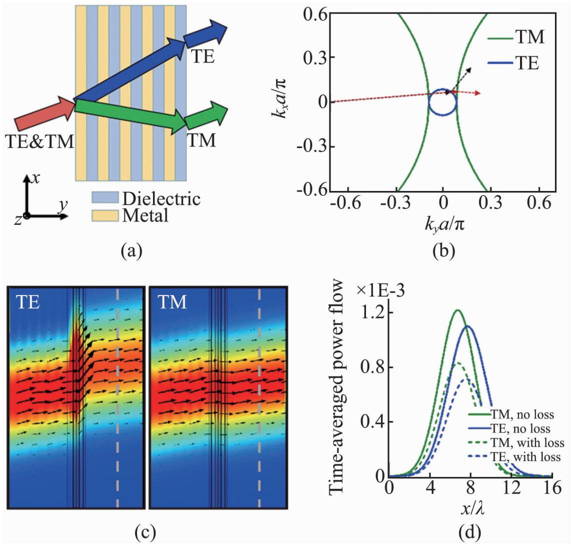

Fig. 2 (a) Schematic of the second kind of PBS. (b) The EFCs for TE (blue lines) and TM (green lines) polarizations. (c) Snapshots of the magnitude (color) and direction (arrows) of the time-averaged power flow for TE (left) and TM (right) polarized waves under an incident angle of θ = 10 deg. The multilayered structure is composed of 5 unit cells and an additional metal layer. (d) The distribution of time-averaged power flow along the dashed lines in (c) for TE (blue lines) and TM (green lines) polarizations. The solid and dashed lines in (d) denote the lossless case with $\varepsilon_m = -2$ and the lossy case with $\varepsilon_m = -2 + 0.02i$, respectively. The relevant parameters are the same as those in Fig. 1

图 2 (a)第二类偏振分光器的示意图. (b)TE 偏振(蓝色曲线)和 TM 偏振(绿色曲线)下的等频率曲线. (c)TE 偏振(左图)和 TM 偏振(右图)电磁波以 10°入射角照射时的平均能流分布图,其中颜色和箭头分别代表平均能流的大小和方向. 该多层结构由 5 个结构单元和额外的一层金属层组成. (d)沿着(c)中虚线上的平均能流大小分布图,其中蓝色和绿色曲线分别代表 TE 偏振和 TM 偏振,实线和虚线对应于无吸收情形 $\varepsilon_m = -2$ 和有吸收情形 $\varepsilon_m = -2 + 0.02i$. 其它相关参数与图 1 中相同

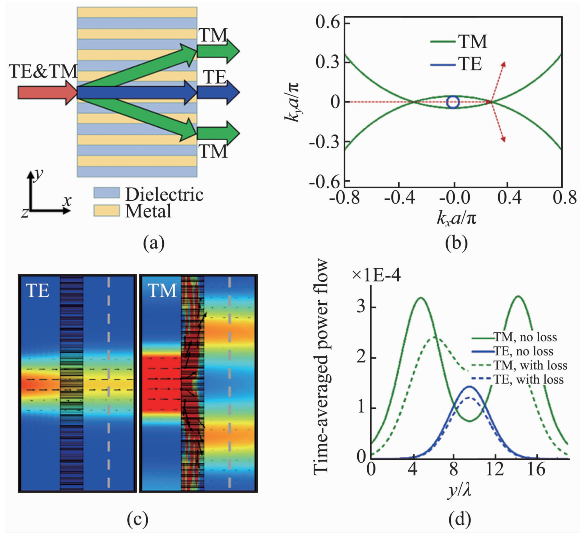

Fig. 3 (a) Schematic of the third kind of PBS. (b) The EFCs for TE (blue lines) and TM (green lines) polarizations. (c) Snapshots of the magnitude (color) and direction (arrows) of the time-averaged power flow for TE (left) and TM (right) polarized waves under normal incidence. The thickness of the multilayered structure is $w = 1.6\lambda$. (d) The distribution of time-averaged power flow along the dashed lines in (c) for TE (blue lines) and TM (green lines) polarizations. The solid and dashed lines in (d) denote the lossless case with $\varepsilon_m = -4$ and the lossy case with $\varepsilon_m = -4 + 0.04i$, respectively. The relevant parameters are $\varepsilon_d = 1$, $f_m = 0.2$ and $a = \lambda/8$

图 3 (a)第三类偏振分光器的示意图. (b)TE 偏振(蓝色曲线)和 TM 偏振(绿色曲线)下的等频率曲线. (c)TE 偏振(左图)和 TM 偏振(右图)电磁波正入射时的平均能流分布图,其中颜色和箭头分别代表平均能流的大小和方向. 该多层结构的厚度为 $w = 1.6\lambda$. (d)沿着(c)中虚线上的平均能流大小分布图,其中蓝色和绿色曲线分别代表 TE 偏振和 TM 偏振,实线和虚线对应于无吸收情形 $\varepsilon_m = -4$ 和 $\varepsilon_m = -4 + 0.04i$ 有吸收情形. 其它相关参数为 $\varepsilon_d = 1$, $f_m = 0.2$ 和 $a = \lambda/8$

The above two kinds of PBSs are based on the separated parabolic dispersion of the TM polarization. Interestingly, the two branches of parabolas can be tuned to be crossed. In Fig. 3, we show that based on the crossed parabolic dispersion, a new kind of PBSs can be achieved. Figure 3(a) illustrates the designed PBS, showing that the normally incident TE polarized waves will propagate through the multilayered structure without refraction. On the other hand, the TM polarized waves split into two beams having symmetric span angles around surface normal. Therefore, the propagation directions of the two polarizations are separated in the simple multilayered structure. The mechanism of the beam splitting for the TM polarization relies on the crossed parabolas (Fig. 3(b)) as the result of surface plasmon-induced nonlocal effect. This means that this kind of PBS is unique and not realizable in metamaterials described by local parameters.

Simulation results are presented in Fig. 3(c), in which the left and right figures correspond to the TE and TM polarizations, respectively. The color (arrows) denotes the magnitude (direction) of the time-averaged power flow. The relevant parameters are $\varepsilon_d = 1$, $\varepsilon_m = -4$, $f_m = 0.2$ and $a = \lambda/8$. It is clearly seen that the TE polarized waves can propagate through the multilayered structure ($w = 1.6\lambda$) without splitting, while the TM polarized wave are symmetrically split into two beams. As a result, there is a wall-off distance in the y direction for the transmitted TE and TM polarized beams, as demonstrated by the distributions of the time-averaged power flow in Fig. 3(d), in which the solid and dashed lines denote the lossless case with $\varepsilon_m = -4$ and the lossy case with $\varepsilon_m = -4 + 0.04i$, respectively. Here, the transmission of this kind of PBSs is not quite high due to the impedance mismatch and material losses, which actually can be relieved by using antireflection layers[56-58] and optical gain media[59-60].

Finally, we note that all the proposed PBSs in the above can be realized in practice. For instance, in 2012, Subramania *et al.* fabricated a Ag-TiO_2 multilayered structure with a near-zero average permittivity in the optical regime[61]. After this work, similar multilayered structures have been fabricated by exploiting Ag and SiN layers[62], Au and SiO_2 layers[63], Ag and SiO_2 layers[64]. These experimental investigations manifest that practical implementation of the proposed PBSs is realizable.

2 Conclusions

In summary, we have proposed three kinds of PBSs by using metal-dielectric multilayered structures based on different dispersions of TE and TM polarizations. The surface plasmon-induced nonlocality results in parabolic dispersion for the TM polarization when the average permittivity is near zero. Interestingly, the designed PBSs can be ultrathin, which may have important applications in compact optical devices.

Acknowledgement

This work is supported by the Shenzhen Science and Technology Plan (Grant No: JSGG20160819150017627, JSGG20160819150000459). Dunjian Wang, Sucheng Li and Wenjie Ji contributed equally to this work.

References

[1] Pendry J B, Holden A J, Stewart W J, *et al*. Extremely low frequency plasmons in metallic mesostructures[J]. *Phys. Rev. Lett.*, 1996, **76**: 4773-4776.

[2] Pendry J B, Holden A J, Robbins D J, *et al*. Magnetism from conductors and enhanced nonlinear phenomena[J]. *IEEE T. Microw. Theory*, 1999, **47**: 2075-2084.

[3] Smith D R, Padilla W J, Vier D C, *et al*. Composite medium with simultaneously negative permeability and permittivity[J]. *Phys. Rev. Lett.*, 2000, **84**: 4184-4187.

[4] Shelby R A, Smith D R, Schultz S. Experimental verification of a negative index of refraction[J], *Science*, 2001, **292**: 77-79.

[5] Pokrovsky A L, Efros A L. Nonlocal electrodynamics of two-dimensional wire mesh photonic crystals[J]. *Phys. Rev.* B, 2002, **65**: 045110.

[6] Belov P A, Marqués R, Maslovski S I, *et al*. Strong spatial dispersion in wire media in the very large wavelength limit[J], *Phys. Rev. B*, 2003, **67**: 113103.

[7] Simovski C R, Belov P A. Low-frequency spatial dispersion in wire media[J]. *Physical Review E*, 2004, **70**: 046616.

[8] Silveirinha M G. Nonlocal homogenization model for a periodic array of ? -negative rods[J]. *Physical Review E*, 2006, **73**: 046612.

[9] Silveirinha M G, Fernandes C A, Costa J R. Additional boundary condition for a wire medium connected to a metallic surface[J]. *New J. Phys.*, 2008, **10**: 053011.

[10] Simovski C R, Belov P A, Atrashchenko A V, *et al*. Wire metamaterials: Physics and applications[J]. *Adv. Mater.*, 2012, **24**: 4229-4248.

[11] Morgado T A, Marcos J S, Costa J T, *et al*. Reversed rainbow with a nonlocal metamaterial[J]. *Appl. Phys. Lett.*, 2014, **105**: 264101.

[12] Brownless J S, Sturmberg B R C P, Argyros A, *et al*. Guided modes of a wire medium slab: Comparison of effective medium approaches with exact calculations[J]. *Phys. Rev. B*, 2015, **91**: 155427.

[13] Elser J, Podolskiy V A, Salakhutdinov I, *et al*. Nonlocal effects in effective-medium response of nanolayered metamaterials[J], *Appl. Phys. Lett.*, 2007, **90**: 191109.

[14] Chebykin A V, Orlov A A, Vozianova A V, *et al*. Nonlocal effective medium model for multilayered metal-dielectric metamaterials[J]. *Phys. Rev. B*, 2011, **84**: 115438.

[15] Chebykin A V, Orlov A A, Simovski C R, *et al*. Nonlocal effective parameters of multilayered metal-dielectric metamaterials[J]. *Phys. Rev. B*, 2012, **86**: 115420.

[16] Sun L, Gao J, Yang X. Giant optical nonlocality near the Dirac point in metal-dielectric multilayer metamaterials[J]. *Opt. Express*, 2013, **21**: 21542-21555.

[17] Chern R L. Spatial dispersion and nonlocal effective permittivity for periodic layered metamaterials[J], *Opt. Express*, 2013, **21**: 16514-16527.

[18] Zapata-Rodríguez C J, Pastor D, Miret J J, *et al*. Uniaxial epsilon-near-zero metamaterials: from superlensing to double refraction[J]. *J. Nanophotonics*, 2014, **8**: 083895.

[19] Chern R L, Han D. Nonlocal optical properties in periodic lattice of graphene layers[J]. *Opt. Express*, 2014, **22**: 4817-4829.

[20] Shen L, Yang T, Chau Y. 50/50 beam splitter using a one-dimensional metal photonic crystal with parabolalike dispersion[J]. *Appl. Phys. Lett.*, 2007, **90**:251909.

[21] Shen L, Wu J, Yang T. Anisotropic medium with parabolic dispersion [J], *Appl. Phys. Lett.*, 2008, **92**: 261905.

[22] Luo J, Xu P, Sun T, *et al*. Tunable beam splitting and negative refraction in heterostructure with metamaterial[J]. *Appl. Phys. A*, 2011, **104**: 1137-1142.

[23] Luo J, Chen H, Hou B, *et al*. Nonlocality-induced negative refraction and subwavelength imaging by parabolic dispersions in metal-dielectric multilayered structures with effective zero permittivity[J]. *Plasmonics*, 2013, **8**: 1095-1099.

[24] Orlov A A, Voroshilov P M, Belov P A, *et al*. Engineered optical nonlocality in nanostructured metamaterials[J]. *Phys. Rev. B*, 2011, **84**: 045424.

[25] Pollard R, Murphy A, Hendren W, *et al*. Optical nonlocalities and additional waves in epsilon-near-zero metamaterials[J]. *Phys. Rev. Lett.*, 2009, **102**: 127405.

[26] Silveirinha M, Belov P. Spatial dispersion in lattices of split ring resonators with permeability near zero[J]. *Phys. Rev. B*, 2008, **77**: 233104.

[27] Forati E, Hanson G W. On the epsilon near zero condition for spatially dispersive materials[J]. *New J. Phys.*, 2013, **15**: 123027.

[28] Kruk S S, Wong Z J, Pshenay-Severin E, *et al*. Magnetic hyperbolic optical metamaterials[J]. *Nat. Commun.*, 2016, **7**: 11329.

[29] Luo J, Yang Y, Yao Z, *et al*. Ultratransparent media and transformation optics with shifted spatial dispersions[J], *Phys. Rev. Lett.*, 2016, **117**: 223901.

[30] Maxwell Garnett J C. Colours in metal glasses and in metallic films [J]. *Philosophical Transactions of the Royal Society A: Mathematical, Physical and Engineering Sciences*, 1904, **203**: 385-420.

[31] Cai W, Shalaev V. *Optical metamaterials: Fundamentals and applications*[M]. Springer, New York, USA, 2009.

[32] Luo J, Lu W, Hang Z, *et al*. Arbitrary control of electromagnetic flux in inhomogeneous anisotropic media with near-zero index[J]. *Phys. Rev. Lett.*, 2014, **112**: 073903.

[33] Luo J, Li J, Lai Y. Electromagnetic impurity-immunity induced by parity-time symmetry[J]. *Phys. Rev. X*, 2018, **8**: 031035.

[34] Luo J, Liu B, Hang Z H, *et al*. Coherent perfect absorption via photonic doping of zero-index media[J]. *Laser Photonics Rev.*, 2018, 2018: 1800001.

[35] Zhang Y, Jiang Y, Xue W, *et al*. A broad-angle polarization beam splitter based on a simple dielectric periodic structure[J]. *Opt. Express*, 2007, **15**: 14363-14368.

[36] Ohtera Y, Sato T, Kawashima T, *et al*. Photonic crystal polarisation splitters[J]. *Electron. Lett.*, 1999, **35**: 1271-1272.

[37] Ao X, Liu L, Wosinski L, *et al*. Polarization beam splitter based on a two-dimensional photonic crystal of pillar type[J]. *Appl. Phys. Lett.*, 2006, **89**: 171115.

[38] Mocella V, Dardano P, Moretti L, *et al*. A polarizing beam splitter using negative refraction of photonic crystals[J]. *Opt. Express*, 2005, **13**: 7699-7707.

[39] Ao X, He S. Polarization beam splitters based on a two-dimensional photonic crystal of negative refraction[J]. *Opt. Lett.*, 2005, **30**: 2152-2154.
[40] Wu L, Mazilu M, Gallet J F, *et al*. Planar photonic crystal polarization splitter[J]. *Opt. Lett.*, 2004, **29**: 1620-1622.
[41] Solli D R, Hickmann J M. Photonic crystal based polarization control devices[J]. *Journal of Physics D*, 2004, **37**: R263.
[42] Solli D R, McCormick C F, Chiao R Y, *et al*. Photonic crystal polarizers and polarizing beam splitters[J]. *J. Appl. Phys.*, 2003, **93**: 9429.
[43] Kim S, Nordin G P, Cai J, *et al*. Ultracompact high-efficiency polarizing beam splitter with a hybrid photonic crystal and conventional waveguide structure[J]. *Opt. Lett.*, 2003, **28**: 2384-2386.
[44] Zabelin V, Dunbar L A, Le Thomas N, *et al*. Self-collimating photonic crystal polarization beam splitter[J]. *Opt. Lett.*, 2007, **32**: 530-532.
[45] Bao Q, Zhang H, Wang B, *et al*. Broadband graphene polarizer[J]. *Nat. Photonics*, 2011, **5**: 411-415.
[46] Chang K, Huang C. Ultrashort broadband polarization beam splitter based on a combined hybrid plasmonic waveguide[J]. *Sci. Rep.*, 2016, **6**: 19609.
[47] Zhao J, Chen Y, Feng Y. Polarization beam splitting through an anisotropic metamaterial slab realized by a layered metal-dielectric structure[J]. *Appl. Phys. Lett.*, 2008, **92**: 071114.
[48] Han C, Tam W Y. Plasmonic ultra-broadband polarizers based on Ag nano wire-slit arrays[J]. *Appl. Phys. Lett.*, 2015, **106**: 081102.
[49] Ma H F, Wang G Z, Jiang W X, *et al*. Independent control of differently-polarized waves using anisotropic gradient-index metamaterials [J]. *Sci. Rep.*, 2014, **4**: 6337.
[50] Ma H F, Wang G Z, Kong G S, *et al*. Independent controls of differently-polarized reflected waves by anisotropic metasurfaces[J]. *Sci. Rep.*, 2015, **5**: 9605.
[51] Li D, Qin L, Xiong X, *et al*. Exchange of electric and magnetic resonances in multilayered metal/dielectric nanoplates[J]. *Opt. Express*, 2011, **19**: 22942.
[52] Grady N K, Heyes J E, Chowdhury D R, *et al*. Terahertz metamaterials for linear polarization conversion and anomalous refraction[J]. *Science*, 2013, **340**: 1304-1307.
[53] Fan R, Zhou Y, Ren X, *et al*. Freely tunable broadband polarization rotator for terahertz waves[J]. *Adv. Mater.*, 2015, **27**: 1201-1206.
[54] Fan R, Liu D, Peng R, *et al*. Broadband integrated polarization rotator using three-layer metallic grating structures[J]. *Opt. Express*, 2018, **26**: 516.
[55] Jia Z, Shu F, Gao Y, *et al*. Dynamically switching the polarization state of light based on the phase transition of vanadium dioxide[J]. *Phys. Rev. Applied*, 2018, 9.
[56] Li Y, Zhang J, Yang B. Antireflective surfaces based on biomimetic nanopillared arrays[J]. *Nano Today*, 2010, **5**: 117-127.
[57] Chen H T, O'Hara J F, Azad A K, *et al*. Manipulation of terahertz radiation using metamaterials[J]. *Laser Photonics Rev.*, 2011, **5**: 513-533.
[58] Luo J, Li S, Hou B, *et al*. Loss/gain-induced ultrathin antireflection coatings[J]. *Sci. Rep.*, 2016, **6**: 28681.
[59] Xiao S, Drachev V P, Kildishev A V, *et al*. Loss-free and active optical negative-index metamaterials[J]. *Nature*, 2010, **466**: 735-738.
[60] Bai P, Ding K, Wang G, *et al*. Simultaneous realization of a coherent perfect absorber and laser by zero-index media with both gain and loss [J]. *Phys. Rev. A*, 2016, **94**: 063841.
[61] Subramania G, Fischer A J, Luk T S. Optical properties of metal-dielectric based epsilon near zero metamaterials[J]. *Appl. Phys. Lett.*, 2012, **101**: 241107.
[62] Maas R, Parsons J, Engheta N, *et al*. Experimental realization of an epsilon-near-zero metamaterial at visible wavelengths[J]. *Nat. Photonics*, 2013, **7**: 907-912.
[63] Gao J, Sun L, Deng H, *et al*. Experimental realization of epsilon-near-zero metamaterial slabs with metal-dielectric multilayers[J]. *Appl. Phys. Lett.*, 2013, **103**: 051111.
[64] Newman W D, Cortes C L, Atkinson J, *et al*. Ferrell-Berreman modes in plasmonic epsilon-near-zero media[J]. *ACS Photonics*, 2015, **2**: 2-7.